RSC Advances

Journal Name

ARTICLE

Organosilica-Metallic Sandwiches Materials as Precursors for Palladium and Platinum Nanoparticle Synthesis

Romain Besnard, Julien Cambedouzou, Guilhem Arrachart*, Xavier F. Le Goff and Stéphane Pellet-Rostaing

A promising strategy to design highly active catalyst is to use multicomponent catalysts including active metals (such as platinoids) and organosilica as substrate. In this article, we develop stable OrganoSilica Sandwiches (OSS) consisting of sandwiched metallic layers between organosilica layers. The formation of such a sandwich-like organosilica@platinoid@organosilica material was obtained from bis-silica-alkylammonium carbamate dimers, acting as a template for the immobilization of platinoid salt complexes or metallic nanoparticles in the interlayer space after a reduction treatment. The layered templates and the sandwich structures were investigated by small angle X-ray scattering, coupled thermogravimetric analysis and mass spectrometry, and Raman spectroscopy. It was demonstrated that the meso-structure of the initial template material is not affected by the chemical steps involved in the synthesis of the material elaboration and does not depend of the incorporated metal.

1. INTRODUCTION

Mesostructured hybrid silicas exhibit singular properties due to the combination of organic–inorganic properties and quantum confinement effects.[1] Tailoring these materials for specific applications, peculiarly metal adsorption[2,3] and catalysis[4,5] requires both compositional and structural control. In particular, materials presenting grafted organic functions able to selectively complex ions are of high interest in the field of solid/liquid extraction, liquid waste processing and metal immobilization.[6,7] Among noble metals, platinoids are well known for their catalytic properties depending of their oxidation state and their crystallographic structure.[8–14] Noble metal NPs are usually prepared by soft templating approaches, using surfactants and organic solvents.[15–20] In these approaches, the shape and size of nanoparticles is driven by the morphology of the organic micelles containing the metallic salt. The use of porous materials as hard templates has been also described.[21–34] The asset of such a method is the better control of the size and the shape of the particles, in particular for the preparation of nanorods.[33]

The use of organosilane precursors is well suited to the preparation of hybrid silica with complexation abilities. Such molecules indeed offer most of the requirements sought for the formation of hybrid organic–inorganic materials, namely a condensable part, and terminal chelating sites with metal adsorption abilities. To get optimal properties, the organically functionalized silica should present a high density of functional groups with a satisfying homogeneity and accessibility. These requirements are usually difficult to obtain with conventional approaches, which consist in post-grafting a functional alkoxysilane on pre-synthesized mesoporous silica, due to the blocking effect at the entrance of the pores.[35] The functionalization by co-codensation is not ideal either recommended because the obtained functional density is weaker and the mesostructure is less defined.

To avoid such drawbacks, an opportunity is to use a bisilylated compound for the preparation of periodic mesoporous organosilica (PMOs), in which organic bridges are incorporated in the three-dimensional network structure of the silica matrix.[36–38] One limitation of this approach may be linked to the weak accessibility of the organic fragments incorporated into the walls, which can be a concern in the field of solid phase extraction. On the other hand, the use of amphiphilic organosilane molecules could be an alternative route in the preparation of a structured functional silica material presenting a high organic function density, as already proposed in a few studies.[39–41]

The organization is specifically driven by the supramolecular assembly process from the organosilane precursors, long-chain alkyl-siloxane with or without self-assembling cross-linker are of particular interest for the design of lamellar bilayer nanostructure.[42-44] These systems have recently been reviewed.[45]

Thanks to the possibilities offered by this approach, amino undecyl-triethoxysilane, which can be considered as an

ARTICLE

amphiphilic organosilane, has been used for the preparation of mesostructured materials starting from their self-assembly into reverse cylindrical micelles or lamellar arrangements.[46,47] Furthermore, the self-assembly of the amino-undecyl-triethoxysilane in pentane or in water with CO_2 as assembly agent led to the formation of bis-silylated-alkylammonium carbamate dimers arranged in a lamellar structure.[46,48]

The removal of CO_2 from ammonium carbamate groups in such materials can easily offered available amino group by heating at moderate temperature.[46,48] The amino group is one of the most attractive surface functionality owing to its use as chelating site for various metal ions. Such affinities for metal anions are particularly increased in acidic aqueous conditions due to the formation of ammonium-metallic salts.

In the present study, we used a similar methodology to incorporate palladium and platinum chloride species at the interface between two bilayers obtained after condensation of silylated amines. The lamellar hybrid material acts as a template for the immobilization in the interlayer space of the platinoid salt, resulting in a stable sandwich-layered structure of organosilica@platinoid@organosilica also called OrganoSilica Sandwich (OSS). The formation of such a sandwich-like material was investigated by Small angle X-ray scattering (SAXS) and microscopy; the exact composition was determined from complementary analyses (elemental analysis, X-EDS, Raman spectroscopy and thermal measurements).

Platinoid salts located inside the impregnated material have been further reduced by thermal treatments without damaging the initial lamellar structure, offering a new approach for the preparation of platinoids nanoparticles based on hybrid silica templating. The combination of microscopy and X-ray scattering techniques allowed us to follow the formation of the crystalline nanoparticles and to highlight unexpected effects on the shape, the size and the distribution of nanoparticles according to the metal immobilized in the material.

2. EXPERIMENTAL SECTION

2.1. Technical details

SAXS experiments were performed on a set-up operating in transmission geometry. A Mo anode associated to a Fox2D multi-shell mirror (XENOCS) delivers a collimated beam of wavelength 0.710 Å. Two sets of scatterless slits[49] delimitate the beam to a squared section of side length 0.8 mm. A MAR345 imaging plate detector allows simultaneously recording scattering vectors q ranging from 0.25 nm^{-1} up to 25 nm^{-1}. Samples were placed in glass capillaries of 2 mm diameter. Absolute intensities were obtained by measuring a calibration sample of high density polyethylene (Goodfellow) for which the absolute scattering was already determined. All SAXS profiles are plotted in log-log scale in order to highlight the dependency of the intensity versus a power law of the scattering vector q.

TEM was carried out at 200 kV on a JEOL 2200 FS microscope. The samples obtained after heat treatment were ground into a powder and dispersed in ethanol. Samples were deposited on 400-mesh carbon-coated copper grids. After ethanol evaporation, the grid was submitted to analysis.

SEM images were obtained from a FEI QUANTA 200 ESEM FEG operating at 15 kV equipped with a Everhart-Thornley detector. X-EDS analyses were performed using a Bruker AXS X-Flash 5010 detector coupled with SEM to quantitatively determine the elementary atomic percentages.

TGA analyses were performed on a Setaram Setsys Evolution 18 instrument under air flow (20 mL.min^{-1}) with a heating rate of 2 °C/min. The coupled mass spectrometer was a Hiden analytical QGA instrument.

Elemental analyses were performed by the Service Central d'Analyse (CNRS, Vernaison, France).

Raman spectra were recorded on a Horiba Jobin Yvon LabRAM Aramis confocal Raman microscope, using an excitation wavelength of λ = 532 nm with a laser spot size of ~1 µm, and with an objective of x50 long working distance. The incident laser power was kept lower than 0.8 mW in order to avoid any heating or structural sample damage.

2.2. Synthesis of amino-undecyl-triethoxysilane

The organic precursor was synthesized in three steps in anhydrous conditions and adapted from the synthesis described in the literature.[50,51] Bromoundecene (Alpha Aesar) was first mixed with triethoxysilane and Karstedt catalyst both purchased from ABCR to obtain bromoundecyl-triethoxysilane. After purification, the organosilane bromide was then condensed with sodium azide (Sigma Aldrich) in acetonitrile to give the expected azidoundecyl-triethoxysilane. Finally, the reduction of the azido group with Palladium (10% Pd / C) from Sigma Aldrich in anhydrous ethanol under hydrogen atmosphere led to amino-undecyl-triethoxysilane.

2.3. Material syntheses

The procedure for preparing the initial material containing a carbamate ammonium salt was adapted from the procedure described by Alauzun *et al.*[46] It was prepared as followed: 3 mmol of amino-undecyl-triethoxysilane (the amphiphilic precursor) were introduced in a 50 mL flask under pure CO_2 gas affording a gel. After 30 min, 20 mL of pentane were poured in the flask and 81 µL of a hydrochloric acid solution was added at pH 1.5. The suspension was stirred for 3 days at 30°C. The resulting material (noted M1) was obtained after filtration. The solid was washed with ethanol and ether before drying under vacuum for 1 hour.

The impregnations of platinoid salts in the materials were performed in aqueous solution. 204 mg of Platinic (IV) chloride hexahydrate ($H_2PtCl_6 \cdot 6H_2O$ purchased from Aldrich) were dissolved in 100 mL of water. The colour of the solution became dark-yellow. 70 mg of Palladium(II) chloride ($PdCl_2$ purchased from Aldrich) were dissolved in 100 mL of a hydrochloric acid solution (pH=1), resulting in a coloured brownish-red solution. Then, 250 mg of M1 material were added in each solution. The resulting mixtures were heated at 70°C for 24h to release the CO_2. Then the resulting solids were filtered and washed with ethanol and ether. After drying under

vacuum for 1 hour, the materials incorporating the platinum salt (noted M1-Pt(IV)) and the palladium salt (noted M1-Pd(II)) were obtained as yellowish and brownish red powders, respectively.

The reduction of impregnated materials was performed through an in situ TGA experiment under 5% H_2 in Argon flow (20 mL.min^{-1}) from 20°C to 140°C. The resulting materials M1-Pt(0) and M1-Pd(0) became respectively dark grey and black.

3. Result and discussion

3.1. Characterization of impregnated materials

The incorporation of platinoid salts has been performed thanks to the release of CO_2 from the pre-formed silica-alkylammonium carbamate M1 material. In order to evaluate the effects of platinoid impregnation in the material, SEM images have been performed before and after impregnation. The morphology and size of the materials were preserved after the impregnation of the platinoid salt solution in the M1 material according to the SEM images (**Figure 1**). The homogeneity of the impregnation was appreciated thanks to the X-EDS analysis. The final composition of the materials will be discussed later.

The SAXS profile of the initial M1 material **(Figure 2a)** can be described by a lamellar meso-structure, where bilayers of bis-aminoundecylsilica are bridged by ammonium carbamate group **(Figure 3)**, and as previously described.[42] The lattice parameter of this lamellar structure can be deduced from the position of the Bragg peaks relative to this lamellar phase (below 10 nm^{-1}) and is estimated at around 3.4 nm. The weak intensity of the first peak indicates that the electronic contrast between the silica matrix and the ammonium carbamate group is rather low **(Figure 3)**.

The largest feature observable at around 15 nm^{-1} (typical distance of 0.42 nm in the real space) can be related to the typical mean lateral distance between two precursors.[47]
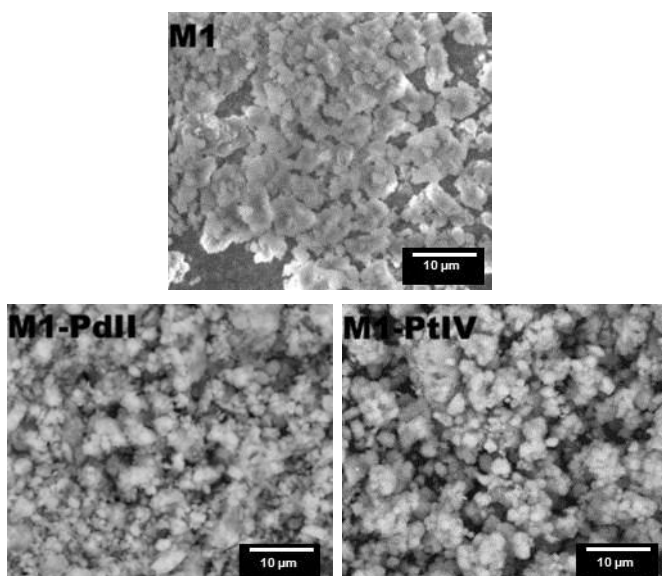

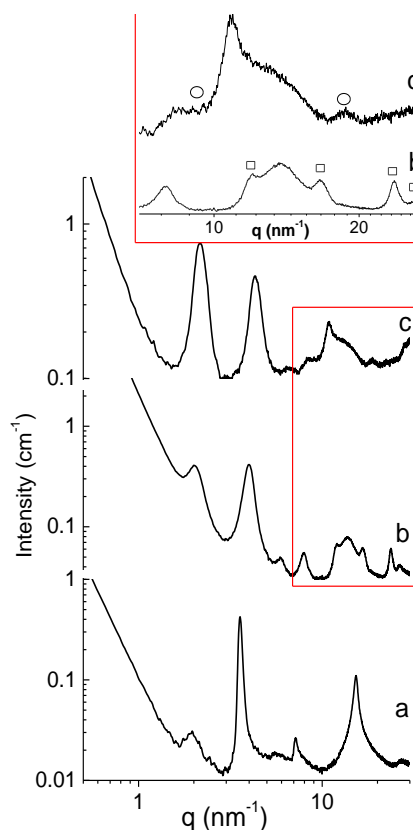Fig. 1 SEM images of the M1, M1-Pd(II) and M1-Pt(IV) materials.

Fig. 2 SAXS profiles of a) M1, b) M1-Pd(II) and c) M1-Pt(IV). The squares and the black rings in the inset correspond respectively to the supplemental structure peaks at wide angles of b) M1-Pd(II) and c) M1-Pt(IV).

The SAXS patterns of both M1-Pd(II) and M1-Pt(IV) powders present a lamellar structure with nearly the same lattice parameter **(Figure 2b,c)**. Therefore, no damage of the lamellar structure is observed due to the incorporation of platinoid salts. Furthermore, the relative intensity of the first peak of the lamellar structure (located at around 2 nm^{-1}) increases after impregnation, especially for the M1-Pt(IV) material.

This suggests that the electronic contrast between the silica matrix and the interface between two bilayers increases.[48]

Therefore, the structural hypothesis of stable sandwich-layered structures consisting in the repetition of stacked sandwiches involving a metal layer between two organosilica layers is likely.

In situ SAXS experiments from room temperature to 120°C have been carried out on the M1 and the M1-Pt(IV) materials **(Figure S1)**. From 70°C, the lamellar structure of M1 material is damaged by CO_2 removal as recently described in a previous study.[48] On the contrary, the lamellar structure of M1-Pt(IV) is maintained even after a similar thermal treatment. This observation is a supplemental indication of the location of platinoid salts inside the lamellar network, and of the contribution of these salts to the cohesion of the lamellar structure. The presence of structure peaks at wide angles was also noticed (localized by circles and squares on **Figure 2b,c**).
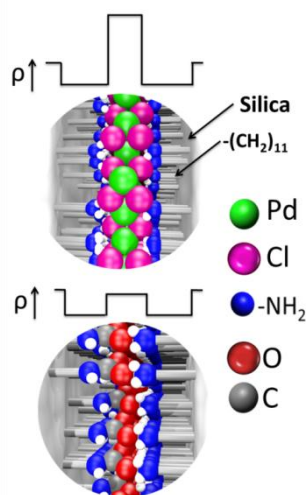
Fig. 3 Schematic representation of the lamellar structure with carbon dioxide or metallic salt at the interface between two organosilica bilayers. The value of the electronic density ρ of each part of the lamellar structure is also represented. Inset: schematic representation of the crystalline monolayer phase of $PdCl_2$ (composed of $PdCl_4^{2-}$ units) at the interface between two organosilica bilayers in the M1-Pd(II) material.
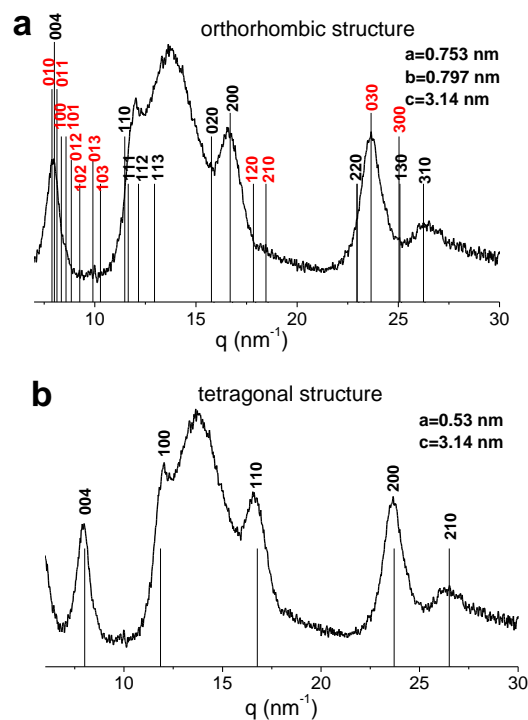

Fig. 4 Calculation of a) the orthorhombic structure and b) the structure tetragonal structure compared to the M1-Pd(II) SAXS profile. The red indexes exhibit Bragg reflections whose indexes h and k are of different parity in the case of the orthorhombic structure.

Their positions correspond to those of a platinoid salt, and the low intensity and the wide shape of the peaks are typical of crystalline nanodomains. M1-Pd(II) was first considered, the SAXS diagram displays four broad peaks located at 11.9 nm^{-1}, 16.7 nm^{-1}, 23.7 nm^{-1}, and 26.2 nm^{-1}. As mentioned in the works of Krishnaswamy et al. in 2006, dealing with a soft crystalline surfactant–Pt(II) complex involving cetyltrimethylammonium bromide (CTAB) as surfactant and chloroplatinate as metallic salt,[15] the formation of a precipitate in a primitive orthorhombic lattice of space group $P222_1$ occurred.

The lattice parameters of this Pt(II)–CTAB complex are a=0.753 nm, b=0.797 nm, c=3.956 nm. The c direction is related to the extended alkyl chains of CTAB molecules, while the a and b direction correspond to distances between Pt atoms. Taking into account the similarity of this system with ours, and provided that the chemical properties of Pd(II) and Pt(II) are close, it appears that such an orthorhombic structure can be considered in order to describe the M1-Pd(II) material. In our case, the material involves silylated-undecylammonium layers instead of CTAB layers. The c lattice parameter should be taken equal to 3.14 nm as determined from the Bragg peak positions indexed in the lamellar structure described above. If the same lattice parameters are considered for the a and b direction in this orthorhombic structure, the Bragg reflections on the planes (010), (011), (100), and (101) should appear between 7.9 and 8.6 nm^{-1}. The broad Bragg reflection on the planes (004) of the lamellar structure does not allow checking the presence of these peaks. However, such a structure should lead to higher order Bragg reflections at 8.85, 9.25, 9.91 and 10.27 nm^{-1}, corresponding respectively to the reflections on the planes (012), (102), (013), and (103) **(Figure 4a)**.

Such peaks do not appear on the SAXS profile. It could be due to the absence of long range correlation in the c direction.

Nevertheless, the Bragg reflections on the planes (120) and (210), expected respectively at 17.84 and 18.45 nm^{-1} are also missing, involving that the hypothetic structure corresponding to a primitive orthorhombic structure is not likely. A face centred C (FC) orthorhombic structure would be in line with the extinction of the Bragg reflections on planes for which h and k indexes are of different parities. In the latter case, the angle between the a and b base vectors would be 86.8°, which is very close to that of a tetragonal structure of lattice parameter a=0.53 nm and c=3.14 nm. In addition, the Bragg reflections on the planes (020) and (021) are not observable, while those of (200) and (201) are visible.

This information leads us to clearly favour the tetragonal lattice of space group P4 with regards to the orthorhombic structure. **Figure 4b** shows that the tetragonal structure gives a better agreement with the experimental data than the orthogonal structure.

Concerning the structure of the M1-Pt(IV) material, no relevant references in the literature were found. Furthermore, its SAXS pattern displays only three broad peaks at 9.2, 10.9 and 18.7 nm^{-1}, making the indexation very delicate. We therefore could not give more detail on the structure of the platinoid salt layer in this material. For both materials, the wide shape and low intensity of the structure peaks could be due to a restrained crystallinity, suggesting that the crystallites are probably very small.

The structural modifications between the initial and the impregnated materials were also observed from TEM micrographs **(Figure 5)**.
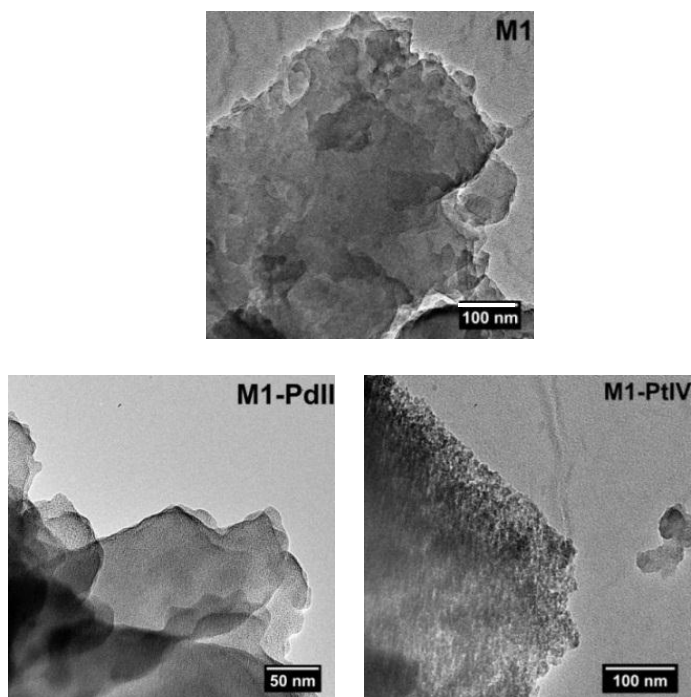
Fig. 5 TEM images of M1, M1Pd(II) and M1Pt(IV) materials

Fig. 6 Thermal analysis (TGA-MS) of a) initial M1 material and b) M1-Pt(IV) material.

From the TEM images, a layered structure is observed for the M1 material, whereas the M1-Pd(II) and M1-Pt(IV) materials show nanodomains that could be platinoid chloride nano-crystallites.

Owing to the differences between the Pt(II)–CTAB complex structure depicted in the literature[15] and that of the M1-Pd(II) material, the composition of both complexes is probably different. In order to evaluate the insertion ratio and confirm our structural hypothesis, thermal analyses coupled with mass spectroscopy of the initial M1 material and the impregnated materials were carried out **(Figure 6)**.

The results for the M1 material show a CO_2 and water release of about 10.5 wt. % between 70°C and 120°C. This departure is almost nonexistent in the case of the M1-Pt(IV) (<1%) material, reflecting the full substitution of the CO_2 by the platinum salt during the impregnation. In addition, the increase of the residual weight at the end of the analysis from 24.8 wt. % to 46 wt. % respectively for the M1 and the M1-Pt(IV) materials confirms the impregnation of the metallic species into the material.

However, considering the possible reduction of the platinum salt even under the air flow, the residual mass at the end of the thermal treatment does not allow the precise determination of the materials composition.

The accurate composition of M1 and M1-Pt(IV) was determined by elemental analysis **(Table 1)**.

While the results for the M1 material give atomic ratios in agreement with that of the undecylamine chain, some inconsistency was observed for M1-Pt(IV). Indeed, the silicon/carbon and silicon/nitrogen atom ratios are respectively 6 and 0.58.
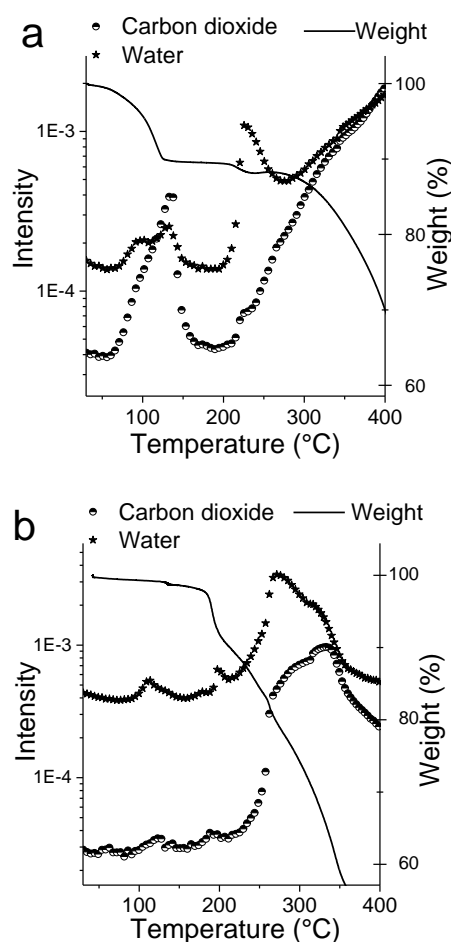
The lack of carbon and nitrogen atoms is probably due to a partial reduction process that occurred during the thermal treatment.

In order to estimate more precisely the amount of platinoid salts into the materials, the elemental analysis results were cross-checked with X-EDS analyses of the impregnated materials M1-Pd(II) and M1-Pt(IV) **(Table 2)**.

According to the X-EDS analyses of M1-Pd(II), the composition was estimated to $(O_xSi-(CH_2)_{11}-NH_2)_{2.6}\cdot PdCl_{2.2}$. The Pd/Cl atomic ratio (measured at 2.18) suggests that the palladium has an oxidation-state of 2.

Table 1: Elemental analysis of M1 and M1-Pt(IV) materials.

	M1		M1-Pt(IV)	
	wt. %	n/Si	wt. %	n/Si
Si	0.11	1.00	0.10	1.00
C	0.55	11.40	0.27	6.00
N	0.05	0.95	0.03	0.58
Cl	-	-	0.17	1.32
Pt	-	-	0.21	0.29

Table 2: X-EDS analysis of the M1-Pd(II) and M1-Pt(IV) materials. Acquisitions were performed on polish pellets on 49 points for M1-Pd(II) and 5 points for M1-Pt(IV).

	M1-Pd(II)		M1-Pt(IV)	
	Cl/Pd	Si/Pd	Cl/Pt	Si/Pt
Atomic mean ratio	2.18	2.56	4.35	2.80
Standard deviation	0.17	0.12	0.27	0.08

Concerning the M1-Pt(IV) material, both elemental and X-EDS analyses proved that the Pt/Cl atomic ratio is included between 4 and 4.5, suggesting that the platinum has an oxidation state of 4 and involving a composition $(O_xSi-(CH_2)_{11}-NH_2)_{2.8}\cdot PtCl_{4.4}$.

In order to confirm these results, Raman spectroscopy has been performed. Three main modes are allowed in the Raman excitation for regular octahedral MX_6 or planar square MX_4 species, namely the symmetric and antisymmetric stretching modes of M-Cl bounds and the bending mode of Cl-M-Cl fragments.[52,53]

Figures 7a and **7b** display the Raman spectra of M1-Pd(II) and M1-Pt(IV) respectively.

For comparison, the platinoid salt precursors are also shown. The α-form of $PdCl_2$ can be viewed as collinear polymeric chains in which each Pd atom alternates with two Cl atoms. The Raman spectrum of $PdCl_2$ **(Figure 7a)** exhibits an intense band at 274 cm^{-1}, corresponding to the symmetric stretching frequency of Pd-Cl bounds.[54] The antisymmetric stretching mode is observable in the foot of the latter band at 290 cm^{-1}. The symmetric bending mode can also be revealed at 144 cm^{-1}, its intensity being lower due to the restrained number of terminal Pd-Cl stretches in this "infinite" chains configuration. The spectrum of M1-Pd(II) does not show the intense band at 274 cm^{-1} anymore, but two intense bands at 288 and 306 cm^{-1} that are assigned to the symmetric and antisymmetric stretching frequency of Pd–Cl bounds.[52,55]

The appearance of the antisymmetric mode could involve that $PdCl_x$ units are not in the "infinite" chains configuration in the material. However, the bending mode usually observed between 160 and 200 cm^{-1} is not present in this spectrum, signifying that the interface between the two bilayers prevents this vibration mode to appear.

Comparatively, the symmetric and antisymmetric stretching frequency of Pt–Cl bounds show up in the spectra of the M1-Pt(IV) sample and that of the $H_2PtCl_6\cdot nH_2O$[53] respectively at 315 and 340 cm^{-1} **(Figure 7b)**.

A supplemental broad band at 150-180 cm^{-1} was also observed for the M1-Pt(IV) sample. The bending mode is thus allowed through the in-plane and out of plane deformation of the $[PtCl_6]^{2-}$ unit. Nevertheless, the weaker intensity of the latter band for M1-Pt(IV) compared to that of $H_2PtCl_6\cdot nH_2O$[50] suggests that the bending mode would be permitted in M1-Pt(IV) by the two supplemental chlorine atoms which would not interact with the interfaces of the material.

Moreover, no additional vibration band were observed in comparison to the original spectra of platinoid salts.
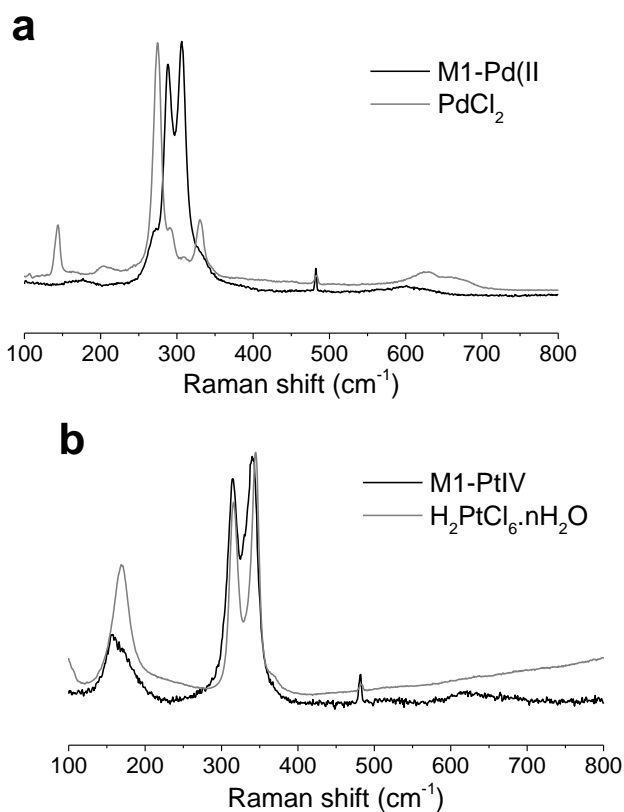

Fig. 7 Raman spectra of a) M1-Pd(II) and b) M1-Pt(IV) and the corresponding metallic salts (respectively $PdCl_2$ and $H_2PtCl_6\cdot H_2O$).

In particular, there is no direct bonding between the metal and nitrogen atoms since the corresponding modes would appear around 500-550 cm^{-1}.[56,57] From these results, we g information on the structure of the platinoid salt inside the lamellar matrix which is in square planar conformation for the palladium salt and in octahedral conformation for the platinum salt.

Finally, to complete the structural study of M1-Pd(II) and give a schematic representation of the structure, the position of the different chemical species inside the lamellar structure had to be determined. Usually, the shortest distance between two Pd inside a classic $PdCl_2$ structure is close to 3.4 Å. Here, this distance is of 5.3 Å, suggesting the insertion of an amine between two Pd atoms. Indeed, the addition of twice the palladium ionic radius (62 pm) and twice the amine radius (200 pm) gives a distance of 5.24 Å, which is in good agreement with the lattice parameter of the tetragonal structure highlighted by the SAXS experiment.

Owing to the M1-Pt(IV) octahedral conformation, the two supplemental chloride out of the plane compared to the M1-Pd(II) could cause the deformation from the tetragonal structure into another structure.

Our structural study thus highlights the unexpected formation of a crystalline monolayer phase at the interface between two organosilica bilayers, leading to an original hybrid mesostructure: a trilayered material composed of an incorporated crystalline monolayer phase of palladium

chloride at the interface between two organosilica bilayers. Such a structure can be described by an ordered packing of organosilica@platinoid@organosilica sandwiches, which we called "OrganoSilica Sandwiches" (OSS) arrangement **(Figure 3)**.

3.2. Thermal reduction effects

The stable sandwich-layered structures described in the paragraph above were subjected to a reduction treatment. The reduction of impregnated materials was performed through an in situ TGA experiment under 5% H_2 in Argon flow (20 mL.min^{-1}) from 20°C to 140°C.

The reduction equation involves the formation of two hydrochloric acids in the case of the palladium salt and four hydrochloric acids in the case of the platinum salt, which can be removed from the material or trapped by the amines contained in the material. In addition, metallic palladium is known for trapping hydrogen. Therefore, the quantitative measurement of the reduction ratio is thus not available by this technique.

We can observe an abrupt weight loss between 60°C and 80°C in the TGA curve **(Figure 8)** of the M1-Pd(II) sample and between 120 and 150°C for the M1-Pt(IV) sample. Considering the composition of M1-Pd(II) as $(O_xSi-(CH_2)_{11}-NH_2)_{2.6}\cdot PdCl_{2.2}$, the loss of two chloride ions during the removal of hydrochloric acid is calculated to 9.3% of the total mass of impregnated M1-Pd(II) material.

The weight losses during this range of temperature have been evaluated to 8% **(Figure 8a)**, in the same range than the calculation, and no supplemental loss was observed after.

In the case of M1-Pt(IV), the removal of four chlorides atoms was estimated to 14.6% which is in agreement with the experiment with a weight loss evaluated to 15.2% from 120 and 150°C (**Figure 8b**).

Therefore, we can consider that the reduction is effective for both materials and the thermal reduction is done with very different behaviours as function of the metallic salt involved.

The resulting materials M1-Pd(0) and M1-Pt(0) became respectively black and dark grey.

The thermal effect on the sandwich-layered structure after reduction has been evaluated by SAXS experiment at room temperature for both impregnated materials **(Figure 9)**.

Firstly, in order to evaluate the thermal effect on the sandwich-layered structure, we focused on the region of scattering vectors q ranging from 1 nm^{-1} to 10 nm^{-1} of the SAXS profiles. The SAXS pattern of M1-Pd(0) displays structure peaks located at 1.95, 3.9, 5.8 and 7.7 nm^{-1} which correspond to the slightly contracted initial lamellar structure of the M1-Pd(II) material.

The intensity of the first structure peak is weaker than that of the material before reduction, but comparable to that of the initial M1 material. This definitely indicates that the electronic contrast between silica planes and the interface of bilayers has come back close to that found in the original lamellar packing of M1.

It could also significate that the palladium salt is not at the interface of bilayers anymore.
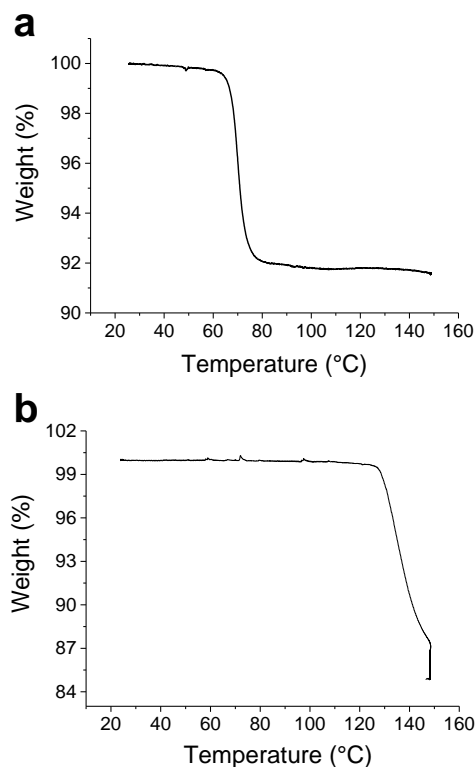

Fig.8 In situ thermal reduction analysis of a) M1-PdII and b) M1-Pt(IV).
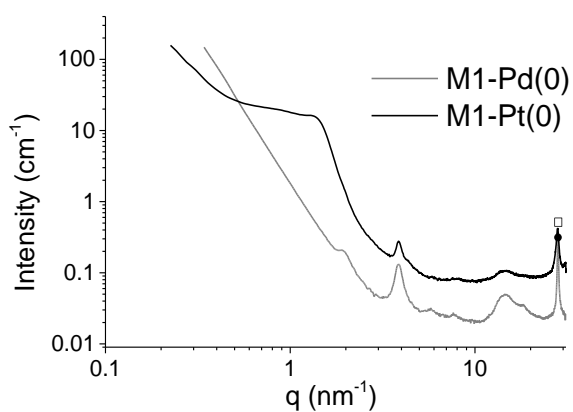

Fig. 9 SAXS profile of samples M1-Pd(0) (grey) and M1-Pt(0) (black). The grey square and the black disk correspond respectively to the first Bragg peak of Pd^0 and Pt^0.

While the M1-Pd(0) SAXS profile seems to present the original lamellar structure, the M1-Pt(0) sample shows a very distinct profile. The structure peak located around 3.9 nm^{-1} is the only remaining peak of the initial lamellar structure. Nevertheless, a broad lump around 1.2 nm^{-1} appears.

This emergence could be due either to a form factor of objects dispersed in the material, or to a structure factor caused by the interactions of nano-sized objects, or to a combination of these two possibilities.

In all cases, the presence of nano-sized objects has to be considered. By focusing on the wider angles on SAXS pattern, we confirm the hypothesis of nano-sized objects. First, the structure peaks characteristic of platinoid salts **(Figure 2)** are missing on both SAXS profiles **(Figure 9)**.

In comparison, only one structure peak is observable at around 28.0 nm^{-1} (marked by a square and a ring respectively for the M1-Pd(0) and the M1-Pt(0) materials in the SAXS patterns displayed in **Figure 9**). Each structure peak is characteristic of metallic palladium and platinum, confirming the effective reduction of platinoid salts.

In order to estimate the platinoid particle size, we applied the Scherrer equation (Equation (1)).

$$t = \frac{k\lambda}{\sqrt{FWHM^2 - s^2}\cos\theta} \qquad (1)$$

where k=0.89 is a standard correction factor, λ=0.71Å is the used wavelength, $FWHM$ is the Full Width at Half Maximum of the peak, s is the instrumental resolution and ϑ is the peak position in radian. ϑ is obtained from the scattering vector q according to the equation (2):

$$q = \frac{4\pi\sin\theta}{\lambda} \qquad (2)$$

The *FWHM* have been calculated from the Voigt fitting equation shown in **Figure S2**.

Table 3 includes the parameters and calculation results for both materials containing the metallic species.

The calculation indicates that palladium particles are larger than platinum particles. The palladium particle size is about 43 nm, while the platinum particles are estimated to 13 nm **(Table 3)**. The above-discussed contribution in the SAXS profile at small angles **(Figure 9)** of the M1-Pt(0) sample could thus be explained by the form factor of such particles, and by the structure factor contribution coming from interactions between these particles. Indeed, the range of observable scattering vector q in the SAXS measurement conditions (0.25 nm^{-1}<q<30 nm^{-1}) allows observing the contribution of particles whose size is smaller than 25 nm.

SEM images of both materials are also very distinct **(Figure 10)**. The M1-Pd(0) image exhibits a layered dappled powder, testifying to the presence of palladium nanoparticles very dispersed inside the material **(Figure 10a)**. The typical size of visible particles is in agreement with that calculated by the Scherrer equation. The M1-Pt(0) image **(Figure 10b)** shows inhomogeneous dispersion of objects whose size is included between 50 and 500 nm.

Table 3: Parameters and calculated size of platinoid particles in impregnated materials.

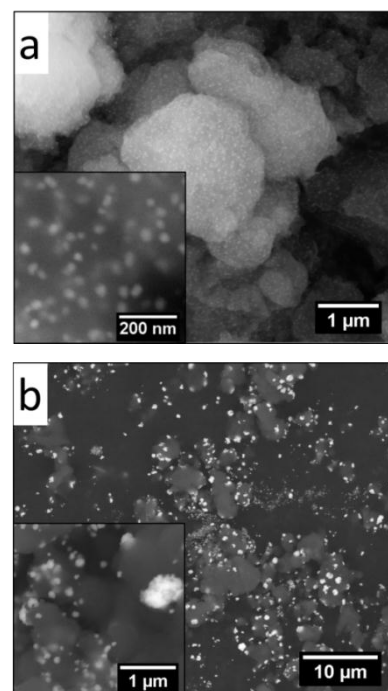|		Pd	Pt
q	nm^{-1}	28.1	28.0
FWHM	nm^{-1}	0.45	0.92
s	nm^{-1}	0.37	0.36
Size	nm	43.1±0.3	13.4±0.2

Fig. 10 SEM images of samples of a) M1-Pd(0) and b) M1-Pt(0).

The TEM images of M1-Pd(0) **(Figure 11a)** shows nanoparticles of different shapes. The **Figure 11b** is a focus on one of them. The particles looks flattened and composed of multi-facets from several merged smaller particles.

The lattice spacing between the (111) planes of metallic Pd is observed in **Figure 11c** at 0.22 nm, which is in good agreement with the distance found in bulk Pd crystal and SAXS results.

The TEM image in **Figure 12** confirms the presence of aggregated nanoparticles in the M1-Pt(0) material.
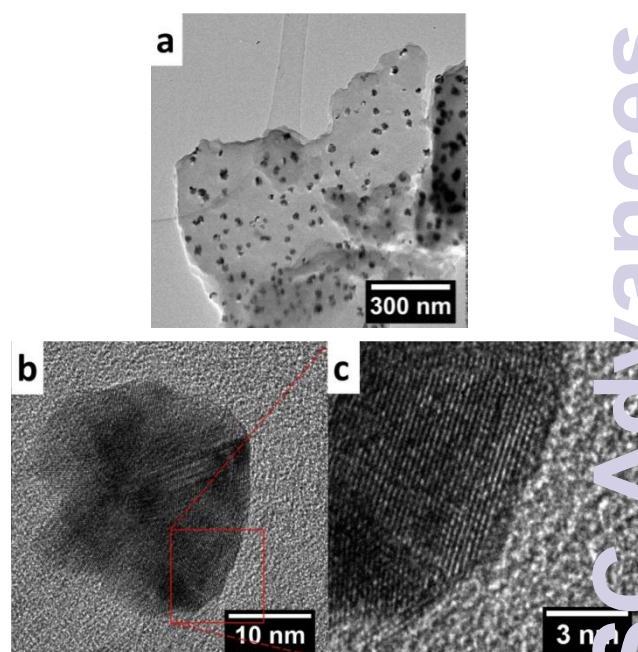

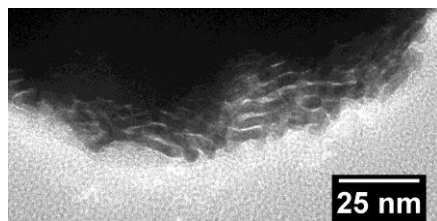Fig. 11 TEM images of sample M1-Pd(0).

Fig. 12 TEM image of sample M1-Pt(0).

The particles appear elongated, like rods aggregated into the interlayer space of the lamellar structure of the M1-Pt(IV) material.

The metallic species seem to have migrated at the extremity of the lamellar network and outside of the material during the reduction **(Figure S3)**. Unfortunately, even if the TEM images illustrated in **Figure S3** exhibit lattice fringes, we could not determine the growth direction of the nanorods due to the limited resolution of the images.

The palladium and the platinum atoms have similar ionic and atomic radius. Furthermore, their crystallographic structure is a face-centered cubic structure (FCC). The differences of size and shape between palladium and platinum nanoparticles is thus likely to arise from the initial oxidation state of platinoid salt precursors (Pd^{2+} and Pt^{4+}). The latter parameter influences the geometry of the initial nanocrystal growing at the interface between the two alkylaminosilica bilayers of the material. Due to this localization, the platinoid salts undergo a confinement effect before the thermal reduction. The square plans composed of $PdCl_4^{2-}$ units result in a reduction toward two directions that further leads to flat aggregates. Oppositely, the structure composed of octahedral $PtCl_6^{2-}$ units could favor the growing up of nanoparticles toward one direction leading to nanorods. Other examples of platinum nanorod growth can be found in the literature. Some syntheses involve SBA15 or MCM-41 silica as cylindrical templates,[21–33] and other soft templating approaches using surfactants and organic solvents result in the synthesis of platinum nanorods from a lamellar mesophase.[15,18,19] Therefore, the shape of the final metallic nanoparticles is not only determined by the geometry of the confinement matrix. Starting from the lamellar structure found in both Pd- and Pt-bearing materials, we demonstrated in this study that the local structure near metallic atoms is determinant for the geometry of the final metal nanoparticles, which could be of planar or rod-like shape.

4. Conclusion

The self-assembly of amino-undecyl-triethoxysilane molecules with carbon dioxide as removable assembly agent is an excellent route to produce hybrid mesostructured lamellar silica. In this article, we develop stable sandwich-layered structures which consist of stacked metal layers between organosilica layers. The formation of such sandwich-like organosilica @ platinoid @ organosilica materials was obtained thanks to bis-silica-alkylammonium carbamate dimers acting as a layered template for the immobilization of

crystalline platinoid salt complexes. These complexes were changed into metallic nanoparticles after reduction treatment. The layered template and sandwich structures, which we called OSS materials, were investigated by SAXS, TGA-MS and Raman spectroscopy. It is showed that the meso-structure of the initial template material is not affected by the different elaboration steps. Due to the combined effects of the confinement and of the crystallographic structure of platinoid salts, the thermal reduction leads to the formation of well-dispersed palladium nanoparticles or to platinum aggregated nanorods. This approach therefore gives access to supported platinoids salts and nanoparticles which can be useful for catalytic applications. Beyond their use as precursors for the preparation of nanoparticles, such ionic hybrid materials could have applications as ionic conductors at low temperature.

Acknowledgements

Notes and references

1   A. P. Alivisatos, *Science* **1996**, *271*, 933–937.
2   G. Arrachart, I. Karatchevtseva, D. J. Cassidy, G. Triani, J. R. Bartlett, M. W. C. Man, *J. Mater. Chem.* **2008**, *18*, 3643–3649.
3   F. Colbeau-Justin, C. Boissière, A. Chaumonnot, A. Bonduelle, C. Sanchez, *Adv. Funct. Mater.* **2014**, *24*, 233–239.
4   A. Zamboulis, N. Moitra, J. J. E. Moreau, X. Cattoën, M. W. C. Man, *J. Mater. Chem.* **2010**, *20*, 9322–9338.
5   W. Otani, K. Kinbara, Q. Zhang, K. Ariga, T. Aida, *Chem Eur J* **2007**, *13*, 1731–1736.
6   R. Turgis, G. Arrachart, C. Delchet, C. Rey, Y. Barré, S. Pellet-Rostaing, Y. Guari, J. Larionova, A. Grandjean, *Chem. Mater.* **2013**, *25*, 4447–4453.
7   A. Charlot, S. E. Mourabit, F. Goettmann, G. Arrachart, R. Turgis, A. Grandjean, *RSC Adv.* **2014**, *4*, 64138–64141.
8   W. Huang, J. Guo, Y. Xiao, M. Zhu, G. Zou, J. Tang, *Tetrahedron* **2005**, *61*, 9783–9790.
9   L. N. Lewis, N. Lewis, *J. Am. Chem. Soc.* **1986**, *108*, 7228–7231.
10 J. Stein, L. N. Lewis, Y. Gao, R. A. Scott, *J. Am. Chem. Soc.* **1999**, *121*, 3693–3703.
11 J. L. Speier, in *Catal. Org. Synth.*, Academic Press, **1979**, pp. 407–447.
12 M. Chauhan, B. J. Hauck, L. P. Keller, P. Boudjouk, *J. Organomet. Chem.* **2002**, *645*, 1–13.
13 C. C. C. Johansson Seechurn, M. O. Kitching, T. J. Colacot, V. Snieckus, *Angew. Chem. Int. Ed.* **2012**, *51*, 5062–5085.
14 Q. M. Kainz, R. Linhardt, R. N. Grass, G. Vilé, J. Pérez-Ramírez, W. J. Stark, O. Reiser, *Adv. Funct. Mater.* **2014**, *24*, 2020–2027.
15 R. Krishnaswamy, H. Remita, M. Impéror-Clerc, C. Even, P. Davidson, B. Pansu, *ChemPhysChem* **2006**, *7*, 1510–1513.
16 G. Surendran, L. Ramos, B. Pansu, E. Prouzet, P. Beaunier, F. Audonnet, H. Remita, *Chem. Mater.* **2007**, *19*, 5045–5048.
17 G. Surendran, F. Ksar, L. Ramos, B. Keita, L. Nadjo, E. Prouzet, P. Beaunier, P. Dieudonné, F. Audonnet, H. Remita, *J. Phys. Chem. C* **2008**, *112*, 10740–10744.

18 F. Ksar, G. Surendran, L. Ramos, B. Keita, L. Nadjo, E. Prouzet, P. Beaunier, A. Hagège, F. Audonnet, H. Remita, *Chem. Mater.* **2009**, *21*, 1612–1617.

19 Y. Song, R. M. Garcia, R. M. Dorin, H. Wang, Y. Qiu, E. N. Coker, W. A. Steen, J. E. Miller, J. A. Shelnutt, *Nano Lett.* **2007**, *7*, 3650–3655.

20 Y.-M. Lu, H.-Z. Zhu, W.-G. Li, B. Hu, S.-H. Yu, *J. Mater. Chem. A* **2013**, *1*, 3783–3788.

21 C. H. Ko, R. Ryoo, *Chem. Commun.* **1996**, 2467–2468.

22 Z. Liu, O. Terasaki, T. Ohsuna, K. Hiraga, H. J. Shin, R. Ryoo, *ChemPhysChem* **2001**, *2*, 229–231.

23 F. Kleitz, S. H. Choi, R. Ryoo, *Chem. Commun.* **2003**, 2136–2137.

24 Z. Liu, Y. Sakamoto, T. Ohsuna, K. Hiraga, O. Terasaki, C. H. Ko, H. J. Shin, R. Ryoo, *Angew. Chem. Int. Ed.* **2000**, *39*, 3107–3110.

25 Y.-J. Han, J. M. Kim, G. D. Stucky, *Chem. Mater.* **2000**, *12*, 2068–2069.

26 L.-X. Zhang, J.-L. Shi, J. Yu, Z.-L. Hua, X.-G. Zhao, M.-L. Ruan, *Adv. Mater.* **2002**, *14*, 1510–1513.

27 C. Yang, P. Liu, Y. Ho, C. Chiu, K. Chao, *Chem. Mater.* **2003**, *15*, 275–280.

28 J. Zhu, Z. Kónya, V. F. Puntes, I. Kiricsi, C. X. Miao, J. W. Ager, A. P. Alivisatos, G. A. Somorjai, *Langmuir* **2003**, *19*, 4396–4401.

29 D. Wang, H. Luo, R. Kou, M. P. Gil, S. Xiao, V. O. Golub, Z. Yang, C. J. Brinker, Y. Lu, *Angew. Chem. Int. Ed.* **2004**, *43*, 6169–6173.

30 S.-H. Liu, R.-F. Lu, S.-J. Huang, A.-Y. Lo, S.-H. Chien, S.-B. Liu, *Chem. Commun.* **2006**, 3435–3437.

31 N. C. King, R. A. Blackley, W. Zhou, D. W. Bruce, *Chem. Commun.* **2006**, 3411–3413.

32 N. C. King, R. A. Blackley, M. L. Wears, D. M. Newman, W. Zhou, D. W. Bruce, *Chem. Commun.* **2006**, 3414–3416.

33 H. Liu, D. Ma, X. Bao, *Dalton Trans.* **2009**, 1894–1896.

34 E. D. Martínez, C. Boissière, D. Grosso, C. Sanchez, H. Troiani, G. J. A. A. Soler-Illia, *J. Phys. Chem. C* **2014**, *118*, 13137–13151.

35 M. H. Lim, A. Stein, *Chem Mater* **1999**, *11*, 3285–3295.

36 T. Asefa, M. J. MacLachlan, N. Coombs, G. A. Ozin, *Nature* **1999**, *402*, 867–871.

37 W. J. Hunks, G. A. Ozin, *J. Mater. Chem.* **2005**, *15*, 3716–3724.

38 P. V. D. Voort, D. Esquivel, E. D. Canck, F. Goethals, I. V. Driessche, F. J. Romero-Salguero, *Chem. Soc. Rev.* **2013**, *42*, 3913–3955.

39 E. Ruiz-Hitzky, S. Letaïef, V. Prévot, *Adv. Mater.* **2002**, *14*, 439–443.

40 R. Voss, A. Thomas, M. Antonietti, G. A. Ozin, *J Mater Chem* **2005**, 4010–4014.

41 Q. Zhang, K. Ariga, A. Okabe, T. Aida, *J Am Chem Soc* **2004**, *126*, 988–989.

42 A. Shimojima, K. Kuroda, *Chem. Rec.* **2006**, 6, 53–63.

43 a) J. J. E. Moreau, B. P. Pichon, G. Arrachart, C. M. Wong Chi Man and C. Bied, *New J. Chem.* **2005**, 29, 653-658. b) G. Arrachart, A. Bendjerriou, C. Carcel, J. J. E. Moreau and M. Wong Chi Man, *New J. Chem.* **2010**, 34, 1436-1440.

44 S. C. Nunes, K. Bürglová, J. Hodačová, R. A. S. Ferreira, L. D. Carlos, P. Almeida, X. Cattoën, M. Wong Chi Man, V. de Zea Bermudez *Eur. J. Inorg. Chem.* **2015**, 1218–1225.

45 A. Chemtob, L. Ni, C. Croutxé-Barghorn, B. Boury, *Chem. Eur. J.* **2014**, 20, 1790–1806.

46 J. Alauzun, E. Besson, A. Mehdi, C. Reye, R. J. P. Corriu, *Chem. Mater.* **2008**, *20*, 503–513.

47 R. Besnard, J. Cambedouzou, G. Arrachart, O. Diat, S. Pellet-Rostaing, *Langmuir* **2013**, *29*, 10368–10375.

48 R. Besnard, G. Arrachart, J. Cambedouzou, S. Pellet-Rostaing, *RSC Adv.* **2015**, *5*, 57521–57531.

49 Y. Li, R. Beck, T. Huang, M. C. Choi, M. Divinagracia, *J. Appl. Crystallogr.* **2008**, *41*, 1134–1139.

50 S. Lambert, K. Y. Tran, G. Arrachart, F. Noville, C. Henrist, C. Bied, J. J. E. Moreau, M. W. Chi Man, B. Heinrichs, *Microporous Mesoporous Mater.* **2008**, *115*, 609–617.

51 B. P. Pichon, M. Wong Chi Man, C. Bied, J. J. E. Moreau, *J Organomet Chem* **2005**, 1126–1130.

52 P. J. Hendra, *Nature* **1966**, *212*, 179.

53 L. A. Woodward, J. A. Creighton, *Spectrochim. Acta* **1961**, *17*, 594–599.

54 M. S. Naz M Aghatabay, *Eur. J. Med. Chem.* **2007**, *42*, 1069–1075.

55 H. Stammreich, R. Forneris, *Spectrochim. Acta* **1960**, *16*, 363–367.

56 J. Pei, X. Li, *J. Solid State Electrochem.* **2000**, *4*, 131–140.

57 D. Michalska, R. Wysokinski, *Chem. Phys. Lett.* **2005**, *403*, 211–218.

Organosilica-Metallic Sandwiches Materials as Precursors for Palladium and Platinum Nanoparticle Synthesis

Romain Besnard, Julien Cambedouzou, Guilhem Arrachart*, Xavier F. Le Goff and Stéphane Pellet-Rostaing

Table of Contents/Abstract Graphics
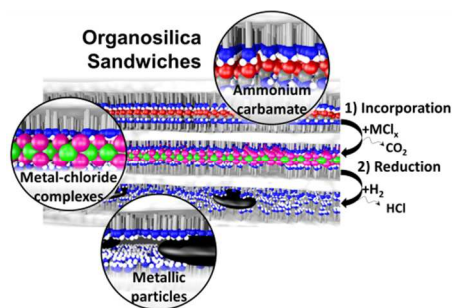
Synthesis of organosilica-metallic sandwiches materials thanks to the immobilization of metallic species in the interlayer space of lamellar bilayer nanostructure.

1